CHEMISTRY OF MATERIALS
Cite This: Chem. Mater. 2019, 31, 3340−3348
Article
pubs.acs.org/cm

Surface Wetting Controls Calcium Carbonate Crystallization Kinetics

Ayumi Koishi,[†,#] Alejandro Fernandez-Martinez,[*,†] Alexander E. S. Van Driessche,[†] Laurent J. Michot,[‡] Carlos M. Pina,[§,∥] Carlos Pimentel,[§,∥] Byeongdu Lee,[⊥] and German Montes-Hernandez[†]

[†]Université Grenoble Alpes, Université Savoie Mont Blanc, CNRS, IRD, IFSTTAR, ISTerre, 38000 Grenoble, France
[‡]Laboratoire Phenix, CNRS−Sorbonne Université−UPMC UMR 8234, 75005 Paris, France
[§]Departamento de Mineralogía y Petrología, Universidad Complutense de Madrid, 28040 Madrid, Spain
[∥]Instituto de Geociencias (UCM-CSIC), 28040 Madrid, Spain
[⊥]Advanced Photon Source, Argonne National Laboratory, Argonne, 60439 Illinois, United States

Supporting Information

ABSTRACT: Because of the widespread presence of foreign substrates in natural settings, mineral precipitation usually occurs via heterogeneous nucleation. This process is controlled by the interplay between the fluid supersaturation and interfacial energies present between the fluid, nucleus, and substrate. Among a number of physicochemical parameters, the surface wetting properties have been shown to be a key parameter controlling heterogeneous nucleation. The present study aims at elucidating the pathway and kinetics of $CaCO_3$ heterogeneous nucleation on a set of phlogopite micas with and without fluorine/hydroxyl substitutions, yielding substrates with contrasting hydrophilicity. Our results show that, irrespective of surface wetting properties, amorphous calcium carbonate (ACC) is formed during the early stages. The surface wetting properties have a strong effect on the crystallization kinetics: ACC precipitates persist longer on the hydrophilic (hydroxylated) surface than on the less hydrophilic (fluorinated) one. We show that this stabilization could have a thermodynamic origin because of the lower interfacial free energy between the hydrated amorphous precursor and the hydrophilic substrate. These results are highly relevant for biomineralization studies, where differences in wetting properties of organic moieties present in calcifying organisms could be used to accelerate or decelerate the crystallization of the initially formed amorphous precursor phase.

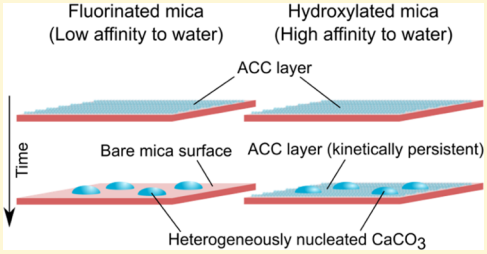

INTRODUCTION

The biogeochemical precipitation and dissolution of alkaline earth and metal carbonates (MCO_3, with M mainly Ca^{2+}, Mg^{2+}, and Fe^{2+}) regulates the composition of natural waters, their alkalinity, and the solubility of other solid phases,[1] controlling the formation of a wide range of minerals, rock alteration processes, as well as the transport and sequestration of contaminants in the subsurface.[2−5] Carbonates, particularly Ca^{2+}, are also one of the major constituents of biominerals that represent an important biotic sink of CO_2.[6−8] In nature, the very first step in the precipitation process, that is, nucleation, usually stems from the interactions of ions with a surrounding matrix of either organic or inorganic origin.[9,10] This process, generally referred to as heterogeneous nucleation, involves molecular-scale dynamics resulting from complex physicochemical interactions between fluid, nucleus, and substrate. In recent years, multistep nucleation pathways—also termed "nonclassical" pathways—have been described.[11−13] These pathways involve intermediates such as clusters, nanocrystals, or amorphous precipitates in the kinetic path from a supersaturated solution to a stable crystalline phase. The case of $CaCO_3$ is paradigmatic: the existence of an amorphous intermediate allows organisms to shape the intricate forms of their shells and skeleton biominerals.[14−17] The biomineral formation also results from a convoluted interplay of factors such as inorganic ions and water,[18,19] proteins and other macromolecules of the organic matrix,[20−23] and their interfaces and the resulting confinements.[24,25] In spite of the relevance of the multistep pathway and the interfacial factors in biomineralization, few studies have been devoted to the elucidation of multistep heterogeneous nucleation pathways.[26,27] This directs our study to the role of interfaces, addressing how their physicochemical properties, particularly the wetting behavior, control the pathway and kinetics of $CaCO_3$ precipitation. Taking into account the omnipresence of foreign interfaces in both natural and engineered media, the outcome of this study is also relevant to geological storage of CO_2,[28,29] scale formation in industrial processes,[30−32] and synthesis of biomimetic materials,[33−35] to name just a few examples.

Experimental characterization of heterogeneous nucleation remains challenging because of the small size of the critical

Received: January 28, 2019
Revised: April 23, 2019
Published: April 24, 2019

DOI: 10.1021/acs.chemmater.9b00417
Chem. Mater. 2019, 31, 3340−3348

nuclei—in the nanometer scale—and to their short lifetimes. The likelihood of heterogeneous nucleation has been primarily attributed to the lattice match between the substrate and the nucleating phase, particularly in solid-state nucleation processes.[36] When it occurs from solution, on the other hand, the height of the nucleation barrier is dictated by complex interactions between local supersaturation, substrate properties, stereochemical compatibility, and other physico-chemical parameters. In such a complex context, substrate hydrophobicity has been demonstrated to be a key parameter[37,38] in controlling heterogeneous nucleation by modifying the energetic interplay within the liquid−substrate−crystal system. The energetic penalty of water adsorption on hydrophobic substrates seems to favor dewetting, which in turn facilitates the precipitation of the solid phase. The effectiveness of this process can also be modulated by the presence and type of charged functional groups that lead to cation binding.[37−40] A popular approach in heterogeneous nucleation studies has been to coat the substrates by different polysaccharides or self-assembled monolayers.[37−40] While this approach provides macroscopically flat surfaces with tuned properties, it neglects the fact that the resulting molecular structure of each of the functionalized surfaces is necessarily different from each other. The nuclei then see different stereochemical environments and the resulting interfacial energetics can vary, preventing the isolated study of specific interfacial parameters, be it either surface hydrophobicity or lattice mismatch.

To specifically address how surface wetting controls the pathway and the kinetics of $CaCO_3$ precipitation, we propose to take advantage of the naturally occurring fluorine (F) substitution in mica minerals, such as phlogopite mica in our case. Hydroxylated and fluorinated phlogopites are abundant mica minerals whose surface properties are closely related to minerals of the clay group: they share a two-dimensional structure with interlayer cations, and a hydrophilic behavior dictated both by the presence of hydroxyl groups and hydrated cations. At varying F substitution ratios, they present high similarity in their surface structures while yielding strikingly different wetting properties. Using these phlogopite mica as substrates (i.e., OH and F phlogopite), we performed heterogeneous nucleation experiments of $CaCO_3$ under different supersaturations. To observe the nucleation process in situ and at the nanoscale, we used grazing incidence small-angle X-ray scattering (GISAXS), a synchrotron-based surface-sensitive technique that has been successfully employed for similar systems.[37,41,42] These data are complemented by ex situ characterization of the nucleated particles with atomic force microscopy (AFM) and infrared spectroscopy, to provide a full mechanistic description of the nucleation process.

MATERIALS AND METHODS

Sample Preparation. Phlogopite micas were used as substrates for all experiments (Table 1). Samples labeled "OH phlogopite" and "$F_{0.8}$ phlogopite" are natural, whereas "F phlogopite" is synthetic. Substrates were cleaved using Scotch tape in ultrapure water to minimize the splitting force, immediately before each measurement.

In Situ Time-Resolved GISAXS. In situ heterogeneous nucleation experiments were performed on OH and F phlogopite micas (Table 1). Freshly cleaved mica substrates were glued on a sample holder with a small amount of crystal bond (Crystalbond 509, Agar Scientific) and fixed horizontally in a custom-made fluid cell (for details see Figure S1A). Equimolar solutions of $CaCl_2$ and $NaHCO_3$ (Table 2) were flowed at a constant rate of 5.7 mL/min using peristatic pumps (model WPX1-NF1/8S4-J8-YP, Welco Co. Ltd., Tokyo, Japan). Both solutions were mixed using a Y-mixer placed at ∼15 cm before the inlet of the fluid cell. Before each measurement, the cell and Teflon tubing were rinsed thoroughly by flowing a 2% HCl solution, followed by ultrapure water, through the setup.

GISAXS measurements were performed at the 12ID-B beamline located at the Advanced Photon Source (Argonne National Laboratory, USA). An incident X-ray energy of 14 keV and a sample-to-detector distance of 2020 mm were selected to cover a q range of 0.002−0.4 Å^{-1}. The incident angle was set slightly lower (α_i = 0.1°) than the critical angle for the total reflection from phlogopite ($\alpha_c \approx 0.14°$ at 14 keV incident energy), allowing the X-ray beam to be reflected by the substrate. GISAXS patterns were collected every 3 min with 30 s of exposure time, for a time frame of 2 to 5 h. To minimize and (if any) verify beam damage, GISAXS patterns at left and right sides of the irradiated spot were collected every 18 min. From time to time, scattering from the solution was also collected to confirm the absence of homogeneous nucleation. Supersaturations (σ = ln(IAP/K_{SP}), where IAP is the ionic activity product and K_{SP} is the solubility product constant) with respect to calcite and amorphous calcium carbonate (ACC) were calculated by Phreeqc[43] using the solubility product constants at 25 °C: $K_{SP(calcite)} = 10^{-8}$[44,48] and $K_{SP(ACC)} = 10^{-7}$,[45,64] as well as the pH values of the two reactants measured before each experiment and the concentrations reported in Table 2.

GISAXS scattering images were corrected by transmission using a monitor value of the incident intensity on the sample and the scattered intensity at the Kapton peak at high q. Horizontal cuts of the scattered intensity were performed along the q_{xy} direction parallel to the plane of the substrate. The intensity along this plane shows an enhancement at the critical angle position because of the Yoneda−Vineyard effect[46] (Figure S1B). For each measurement, the first image (substrate in contact with ultra-pure water, before the mixed solution reaches the fluid cell) was used as background and was subtracted from the rest. The extracted one-dimensional curves (q_{xy} direction) were fitted using the IRENA package installed on Igor Pro 7.02. The "Unified fit", a simple model based on the unified scattering theory,[47,48] was employed in the Guinier region to extract average radius of gyration, R_g, with a Porod slope, s, fixed at $s = -2$ which provided the best fitting results. The GISAXS scattered intensity is proportional to the number density of the particles N/V, where V is the total volume irradiated by the X-ray, the inhomogeneity in the electron densities is $\Delta\rho$, as well as the form factor is $P(q)$ and the structure factor is $S(q)$

Table 1. Summary of Mica Minerals Used as Substrates for Heterogeneous Nucleation Experiments[a]

name	composition	source
OH phlogopite	$(K_{0.98}Na_{0.10})(Mg_{2.44}Al_{0.22}Fe_{0.10}Ti_{0.04}\square_{0.2})(Si_3Al_1)O_{10}(OH)_2$	Jussieu collection, Paris, France
F phlogopite	$KMg_3(AlSi_3O_{10})F_2$	H. C. Materials Corporation, IL, USA
$F_{0.8}$ phlogopite	$(K_{0.96}Na_{0.04})(Mg_{2.74}Fe_{0.16}Al_{0.09}Ti_{0.04})(Si_{2.89}Al_{1.11})O_{10}(OH_{0.46}F_{1.54})$	National Museum of Natural History, Paris, France

[a]OH phlogopite and $F_{0.8}$ phlogopite are natural and F phlogopite is synthetic.

Table 2. Summary of Solution Chemistry Used for Heterogeneous Nucleation Experiments

condition	$\sigma_{calcite}$	σ_{ACC}	$[Ca^{2+}]$ (mM)	$[HCO_3^{2-}]$ (mM)	pH
I	3.97	2.04	15	15	8.27
II	2.97	1.04	10	10	8.10
III	2.67	0.74	7.5	7.5	8.18
IV	2.21	0.28	5	5	8.29

DOI: 10.1021/acs.chemmater.9b00417
Chem. Mater. 2019, 31, 3340−3348

$$I(q) = \frac{N}{V}\Delta\rho^2 V_p^2 P(q) S(q) \quad (1)$$

Provided the absence of defined correlations (no observable peaks in the intensity) and the polydispersity of the particles formed, we assume $S(q) = 1$.

In the framework of the classical nucleation theory (CNT), heterogeneous nucleation is driven by two opposing factors, the supersaturation σ and the effective interfacial energy α', that determine the height of the nucleation barrier Δg_n, which in turn controls the nucleation kinetics. The nucleation rate J_n is then expressed as

$$J_n = \exp\left(\frac{\Delta g_n}{k_B T}\right) = A \exp\left(-\frac{8\pi\Omega^2\alpha'^3}{3k_B{}^3T^3\sigma^2}\right) \quad (2)$$

where k_B is the Boltzmann constant, T is the temperature, A is a kinetic factor related to kinetic pathways, and Ω is a molecular volume (for the two phases assumed, calcite and ACC, experimentally obtained values were 6.13×10^{-29}[49] and 9.03×10^{-29} m^3/mol,[50] respectively). To quantify the nucleation rate, the value of the scattered intensity at $q = 0$ (extrapolated from the unified fit curves) is used and plotted against the evolved time (Figure S2). Because R_g is found to be in the same size range over time (see Results), V_p can be assumed to remain constant and $P(q = 0) = 1$ by definition, it is safe to consider that the $I(q = 0)$ is proportional to the total number of particles N and to the density difference (contrast)

$$I(q = 0) \propto N(\rho_{particle} - \rho_{water})^2 \quad (3)$$

Note that because CNT assumes the first nucleating phase to be identical to the final phase (so-called capillary approximation), the density contrast $(\rho_{partile} - \rho_{water})$ is assumed to be constant over time, which makes $I(q = 0)$ to be solely proportional to the total number of particles N. The nucleation rate J_n can therefore be extracted from the $I(q = 0)$ versus time plots by linear regression (Figure S2). We would like to point out that the so-called SAXS invariant Q method was not applicable to our case because the integral $(\int_0^\infty I(q)q^2\,dq)$ could not converge to zero as it is the case for when the high q data varies as q^{-4}. A regression analysis of the plot $\ln(J_n)$ versus the inverse of σ^2 provides the coefficient estimate that is proportional to the effective interfacial energy α'. For the σ range selected in the present work, linear regression was performed. The effective term α' comprises three components corresponding to the interfacial energies governing the interface between liquid and crystal (α_{lc}), liquid and substrate (α_{ls}), and substrate and crystal (α_{sc})

$$\alpha' = \alpha_{lc}\frac{2(1 - \cos\theta) - \sin^2\theta\left(\frac{\alpha_{ls} - \alpha_{sc}}{\alpha_{lc}}\right)}{2^{1/3}(2 - 3\cos\theta + \cos^3\theta)^{2/3}} \quad (4)$$

where θ is the angle formed between the substrate and the crystal.

Ex Situ Heterogeneous Nucleation Experiments. *Atomic Force Microscopy.* Freshly cleaved substrates (OH and $F_{0.8}$ phlogopite) were fixed on a sample holder using a small amount of Araldite epoxy and placed vertically in a freshly mixed supersaturated solution (condition IV Table 2). After performing several tests at higher supersaturation conditions, relatively low supersaturation was chosen to increase the induction period and also to allow sufficient spacing between the heterogeneously nucleated particles. After 15 min of reaction, the substrates were gently rinsed with ethanol to quench the reaction before being mounted in the observation cell of the AFM (Nanoscope IIIa MultiMode, Veeco Instruments). Topography, vertical deflection and lateral deflection signals were recorded in contact mode in a closed fluid cell, using Bruker SNL-10D tips. The cell was filled with ethanol during data collection to quench the reaction while achieving a better resolution than when exposed in air. The scan areas varied between 10×10 nm^2 and 14×14 μm^2. The scan velocity was set at 5 Hz and was increased to 61 Hz for high-resolution images. Scan quality yields 512 points per line and 512 lines per image. Data analyses were performed using WSxM 4.0 Beta 8.2[51] and NanoScope Analysis 1.50. Normal force F_N was calculated using the following equation:[52]

$$F_N = K_N S_Z V_N \quad (5)$$

where K_N is the normal spring constant (0.06 N/m), S_Z is the sensitivity of the photodetector (m/V), and V_N is the normal voltage (V). For each area scanned, S_Z and V_N values were linearly extrapolated based on the two force distance curves, measured before and after the corresponding scan.

Attenuated Total Reflectance Fourier Transform Infrared Spectroscopy. Freshly cleaved substrates (OH and F phlogopite) were placed vertically in a freshly mixed supersaturated solutions (conditions I, II, and III, Table 2). The substrates were sampled at 1, 3, and 6 h (1 and 3 h for conditions I and II) and gently quenched with ethanol and characterized by attenuated total reflectance Fourier transform infrared spectroscopy (ATR−FTIR) (Nicolet iS10). Spectra were collected in the range of 650−4000 cm^{-1}, by averaging 500 scans at a resolution of 4 cm^{-1} for each measurement. Experiments were performed at least three times for each condition, and the averaged data are shown. Under condition III, the closest solution chemistry as the one (condition IV) employed for AFM observation which provides sufficient FTIR signal, nucleation experiments were repeated and the substrates were sampled after 4 days of reaction for comparison purposes and long-term effects.

RESULTS

In Situ Time-Resolved GISAXS. Time-resolved GISAXS scattered intensity along the so-called Yoneda wing (see Materials and Methods) reflects density fluctuations due to $CaCO_3$ heterogeneous nucleation. Representative time-resolved plots of the horizontally extracted intensity, $I(q)$ versus q, are shown in Figures 1A and S3. After a certain induction time, the scattered intensity increases during the course of the measurement as $CaCO_3$ is formed on the substrate. The length of the induction period varies with substrate type and bulk solution supersaturation. Figure 1B shows a representative fit to the high q region of the data, from which a mean particle size (radius of gyration, R_g) can be obtained.

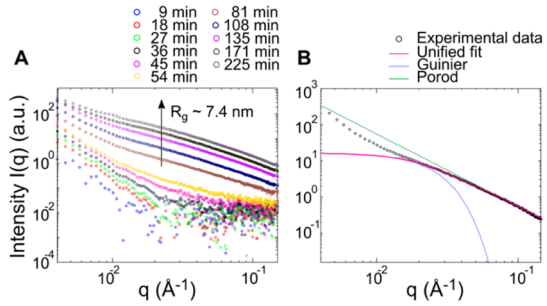

Figure 1. (A) Representative evolution of the GISAXS intensity over time. Data shown here are horizontal cuts at the interface for the $CaCO_3$−F phlogopite system under condition II ($\sigma_{calcite} = 2.97$; $\sigma_{ACC} = 1.04$). (B) Representative fit to the data and Guinier and Porod functions in the high q region. Only the q range where the data display significant statistics is shown (0.004−0.15 $Å^{-1}$, corresponding to a d_{min} of 4.2 nm and a d_{max} of 157 nm).

For both OH and F systems, R_g remained in the same range of values ($R_g \approx 5-7$ nm) for the duration of the experiments (Figure 2A,B). The exception is the F phlogopite system under condition I, where an apparent growth of particles was observed with a R_g value reaching 11 nm. Because R_g remains roughly constant for the tested range of conditions, the increase in intensity is attributed to an increase in the number

DOI: 10.1021/acs.chemmater.9b00417
Chem. Mater. 2019, 31, 3340−3348

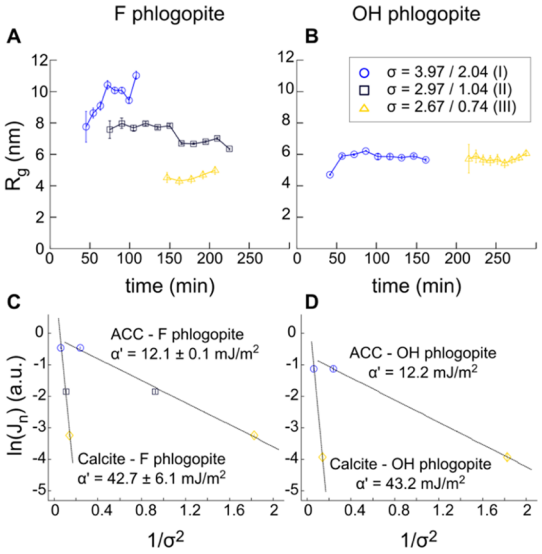

Figure 2. (A,B) Evolution of the radius of gyration (R_g) of $CaCO_3$ particles formed on F and OH phlogopite at different supersaturations ($\sigma_{calcite}/\sigma_{ACC}$). (C,D) Effective interfacial free energies α' for F and OH phlogopite under the hypotheses that calcite and ACC are the nucleated phases. The uncertainties are represented as standard error of linear regression slope. Error bars represent 95% confidence intervals.

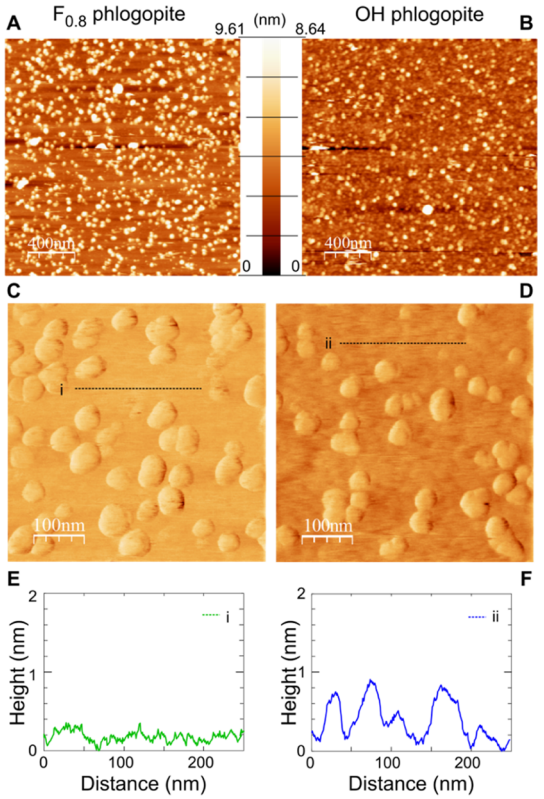

Figure 3. AFM images of $F_{0.8}$ phlogopite and OH phlogopite after 15 min of reaction under condition IV ($\sigma_{calcite}$ = 2.21; σ_{ACC} = 0.28). (A,B) Topography and (C,D) zoomed-in friction images of heterogeneously nucleated $CaCO_3$ particles. (E,F) Height profiles along the dotted lines shown in (C) (i) and (D) (ii) extracted from the corresponding topography images (data not shown).

of particles (i.e., the precipitation process is dominated by nucleation rather than by aggregation or particle growth). This can be best represented by the intensity at $q = 0$ (refer to Materials and Methods), of which the time dependence, $I(q = 0)$ versus time, provides the nucleation rate J_n (Figure S2). Using eq 2, the corresponding effective interfacial free energies (α') were calculated with respect to calcite and ACC, two possible phases considered here as they are the least and the most soluble phases among those susceptible to nucleate. The obtained values of α' were identical for both surfaces (OH and F phlogopite): $\alpha'_{calcite} \approx 43$ mJ/m^2 and $\alpha'_{ACC} \approx 12$ mJ/m^2 (Figure 2C,D). As an independent validation, α' values were also determined using the induction times estimated from the same $I(q = 0)$ versus time plots (Figure S2), yielding slightly different results (Figure S4). We tentatively ascribe this difference to the uncertainty in determining the induction times using $I(q = 0)$ versus time plots. Therefore, the α' values derived from the nucleation rates are considered in the rest of the manuscript.

Ex Situ Observation by AFM. Random and dense populations of $CaCO_3$ particles were observed on both OH and F substrates after 15 min of reaction under condition IV (Figure 3). Substrates were placed vertically during the reaction time to avoid deposition of homogeneously nucleated particles. Most of the particles observed on the surface were not removable after several scans at a maximum applied force of 50 nN (normal force), indicating that they formed via heterogeneous nucleation. A few large aggregated particles were also present on some of the substrates. They were assumed to have been deposited onto the surface after being homogeneously nucleated because they were weakly attached to the surface and were readily removed after a few scans at a low applied force, ~0.5 nN (normal force).

As shown in Figure 3A,B, on average, the particles on OH phlogopite were smaller [46.3 ± 1.9 nm wide and 4.6 ± 0.3 nm high (95% confidence interval)] than those on $F_{0.8}$ phlogopite [57.5 ± 1.9 nm wide and 5.6 ± 0.3 nm high (95% confidence interval)]. In addition, the friction images and the height profiles clearly show that for $F_{0.8}$ phlogopite, the areas in between the $CaCO_3$ particles remain atomically flat (Figure 3C,E), while for OH phlogopite the corresponding areas seem covered by a rough layer of, presumably, $CaCO_3$ (Figure 3D,F). Additional supporting images and the corresponding height profiles are shown in Figure S5. Figure 4 compares high-resolution images of phlogopite surfaces before and after the heterogeneous nucleation events. The two-dimensional fast Fourier transform (FFT) obtained from a bare OH phlogopite surface exhibits a hexagonal pattern (Figure 4A,B). The corresponding unit cell distances are in accordance with the surface structure of this mineral.[53] Figure 4C shows a $F_{0.8}$ phlogopite surface with a heterogeneously nucleated $CaCO_3$ particle. The zoomed area (Figure 4D) displays the characteristic surface structure of phlogopite (001) as confirmed by 2D FFT (inset). To the contrary, the zoomed area of an OH phlogopite surface with heterogeneously nucleated particles does not display a recognizable surface structure as also shown by the corresponding 2D FFT (Figure 4E,F). This, together with the high roughness of the interparticle areas, further supports the idea that the OH surface is entirely covered with a heterogeneously formed layer of $CaCO_3$ precipitates. It must be pointed out that the heterogeneously nucleated particles shown in Figure 4E have experienced a certain degree of wear and are therefore smaller than the original particles, as a result

DOI: 10.1021/acs.chemmater.9b00417
Chem. Mater. 2019, 31, 3340−3348

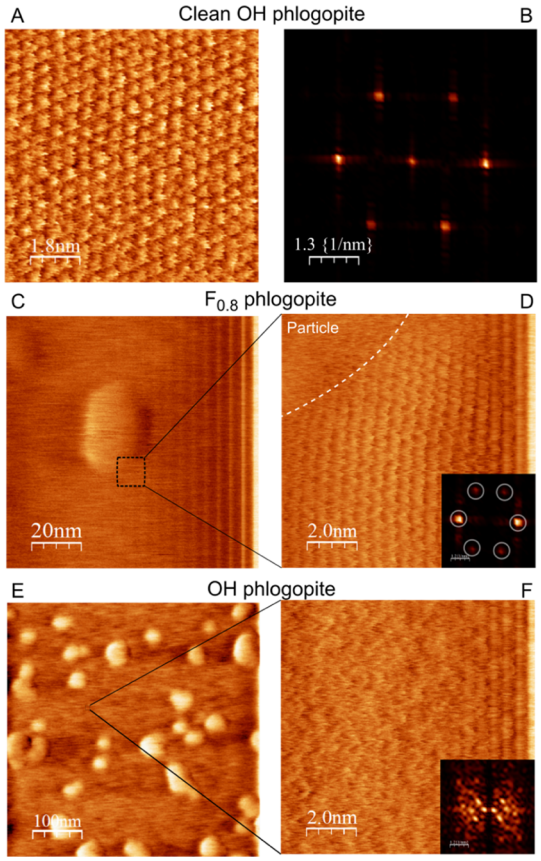

Figure 4. (A) High-resolution friction image of a clean OH phlogopite surface under water before the start of a precipitation experiment, and (B) the 2D FFT showing a hexagonal pattern. (C) High-resolution friction image of $F_{0.8}$ phlogopite surface after a precipitation experiment showing a heterogeneously nucleated $CaCO_3$ particle and (D) a high-resolution friction image with 2D FFT. (E) Friction image of the OH phlogopite surface after the experiment with heterogeneously nucleated $CaCO_3$ particles and (F) a high-resolution friction image with 2D FFT. Condition IV ($\sigma_{calcite}$ = 2.21; σ_{ACC} = 0.28).

of our attempt to expose the unaltered OH phlogopite surface (Figure S6).

Ex Situ Analyses by ATR−FTIR. ATR−FTIR absorbance spectra are used to identify the nucleating phases of the precipitates. Figure 5 shows the FTIR spectra of OH and F phlogopite before and after nucleation experiments under condition III. Before the experiments, the spectra of OH and F phlogopite are comparable to each other except for the region above 3000 cm^{-1} (Figure 5A). OH phlogopite is characterized by a doublet peak at ∼3711 and ∼3670 cm^{-1}, attributed to the structural (octahedral) hydroxyl group,[54,55] and a small feature due to adsorbed water between 3600 and 3000 cm^{-1} (Figure 5A inset). F phlogopite, on the other hand, lacks such features, which is in accordance with previous studies.[56,57] The region below 1000 cm^{-1} is dominated by the strong phlogopite signal, and consequently peak assignments for $CaCO_3$ polymorphs were performed from 1800 to 1200 cm^{-1}.

Spectra of ACC are typically characterized by a split peak of the asymmetric stretch of CO_3^{2-} (ν_3) at ∼1417 and ∼1475 cm^{-1},[19] accompanied by a peak of in-plane bending (δ) of O−H, arising from the structural water of ACC (∼1645 cm^{-1}).[59−61] Such features were observed on OH phlogopite after 1, 3, and 6 h (Figure 5B) and up to 4 days of reaction

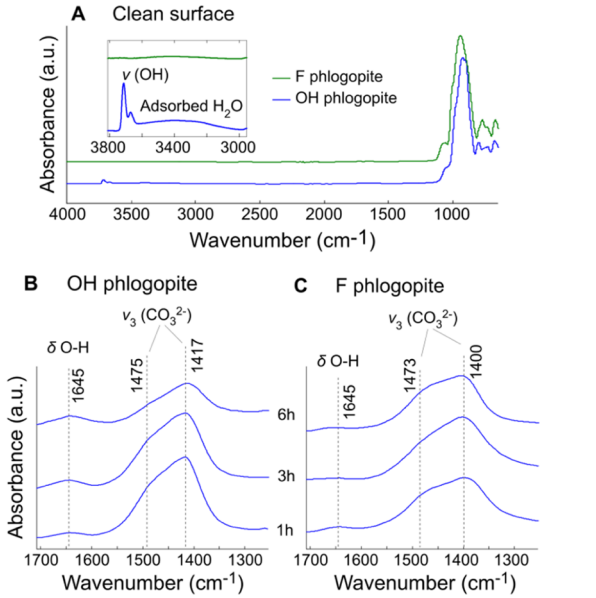

Figure 5. ATR−FTIR normalized absorbance spectra (A) before and (B,C) after 1, 3, and 6 h of reaction under condition III ($\sigma_{calcite}$ = 2.67; σ_{ACC} = 0.74) for OH and F phlogopite. Intensity is normalized to the unity within the *x*-axis limits shown.

with a supersaturated solution of $CaCO_3$ (Figure S7A). In contrast, for F phlogopite, the ν_3 peak mainly occurs at 1400 cm^{-1} (Figure 5C), corresponding to calcite,[19,59,62] with a small shoulder at ∼1473 cm^{-1}. Given the presence of δ O−H at 1645 cm^{-1} at 1 h, the nucleated phase can be identified as a mixture of ACC and calcite. The spectra at 3 and 6 h are tentatively interpreted as corresponding to a mixture of vaterite and calcite based on the absence of δ O−H signals and on the shape of the ν_3 peak.[58]

The transformation of ACC into vaterite on F phlogopite becomes clearer on the 4 day spectrum (Figure S7A) by the shape of ν_3[63,64] and further supported by the presence of both out-of-plane and in-plane bending of CO_3^{2-} (ν_2 and ν_4, respectively) corresponding to vaterite and calcite (715, 742, and 872 cm^{-1}, data not shown). Under conditions I and II (Figure S7B), the spectra exhibit similar trends as condition III, with reactions that proceed faster. ACC is therefore observed in both systems, but with faster crystallization kinetics toward vaterite and calcite in F phlogopite.

DISCUSSION

Effect of Surface Wetting on α' Values. The in situ time-resolved GISAXS experiments show that nucleation of nanometer-scale $CaCO_3$ particles (R_g values range from 4 to 11 nm) occurred for all systems under the investigated experimental conditions (Figure 2A,B). Minor growth of those particles was only observed for F phlogopite under condition I (Figure 2A). The relatively simple method (i.e., Guinier approximation) used to determine R_g values does not provide information about the polydispersity of the formed particles. Hence, the error bars plotted in Figure 2A,B correspond to errors of the average particle size. Within the framework of CNT, the size of the critical clusters is inversely proportional to supersaturation.[9] No such dependence can be seen in both systems (Figure 2A,B), suggesting that the observed particles are not critical clusters. It is worth noting that, though with very low counts (poor statistics), a plateau

DOI: 10.1021/acs.chemmater.9b00417
Chem. Mater. 2019, 31, 3340−3348

was observed in the higher q region in some experimental conditions (data not shown), from which the existence of even smaller particles can be inferred. Nevertheless, the nucleation rate, J_n, (derived from the nanometer-scale particles observed) trends can be fitted using the master equation of CNT (eq 2). This suggests that, even if these particles are not necessarily critical clusters, the aggregation kinetics of these particles provides a good proxy to study nucleation events and their properties.

Application of CNT to the obtained nucleation rates J_n yielded unexpectedly identical values of α' for F and OH phlogopite (Figure 2C,D). This infers that the height of the nucleation barrier is the same in both systems, suggesting that the nucleation mechanism may be the same, irrespective of the surface wetting properties. To this point, the ATR−FTIR data provide the evidence that ACC is present during the early stages of precipitation on both substrates. This observation is further supported by the fact that the scattered GISAXS intensity varies as q^{-2}, from which Porod low indicates a highly porous and polymeric structure,[48,65] possibly referring to ACC. We therefore postulate that in both systems ACC is initially formed through the aggregation of small amorphous clusters which themselves were not directly observed.

Surface Wetting Controls the Stability of ACC. The roughness of the OH phlogopite surface in between the heterogeneously nucleated particles (Figure 3D,F) indicates the presence of a continuous layer, identified as ACC (Figure 5B), that is only partially removable by the AFM tip (Figure S6). The $F_{0.8}$ phlogopite surface, on the other hand, displays a contrasting behavior: a bare surface was found between the heterogeneously nucleated particles (Figures 3C,E and 4C,D) and the formation of ACC was only observed at early nucleation stages (Figure 5C). This is further justified by the formation of vaterite (Figure S7A) that usually forms via ACC.[61,66−68]2 These results consequently point to a shorter lifetime of the ACC layer on F phlogopite compared with that formed on OH phlogopite (Figure 6).

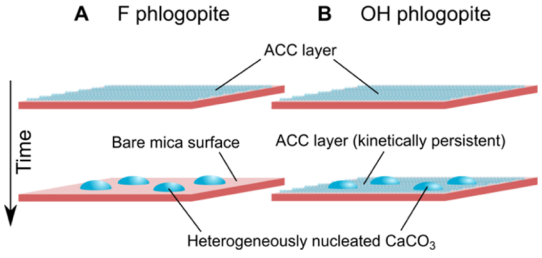

Figure 6. Schematic representation of $CaCO_3$ crystallization kinetics as heterogeneously nucleated on (A) F phlogopite surface and (B) OH phlogopite surface.

This enhanced metastability of the ACC layer may also explain the promoted particle growth on the F phlogopite (Figure 2A), presumably through a dissolution−reprecipitation process upon energetic penalty at the hydrous ACC−F phlogopite interface (α_{sc}). Following this rationale, a plausible scenario for the enhanced kinetic persistence of ACC on OH phlogopite, taking into account its hydrophilicity, could be the formation of hydrogen bonds between the water molecules of ACC and the basal oxygen atoms of the substrate.

Can There be a Thermodynamic Contribution to the Stability of ACC Controlled by Surface Wetting? Our results show that, in the framework of CNT, the surface wettability does not affect the absolute values of effective interfacial energy (α'). However, α' results from a complex interplay between the three interfacial energies emerging during surface-mediated nucleation and contact angle between the substrate and nuclei (eq 4). To fully investigate this complex relation, a 3D thermodynamic diagram (Figure 7) was

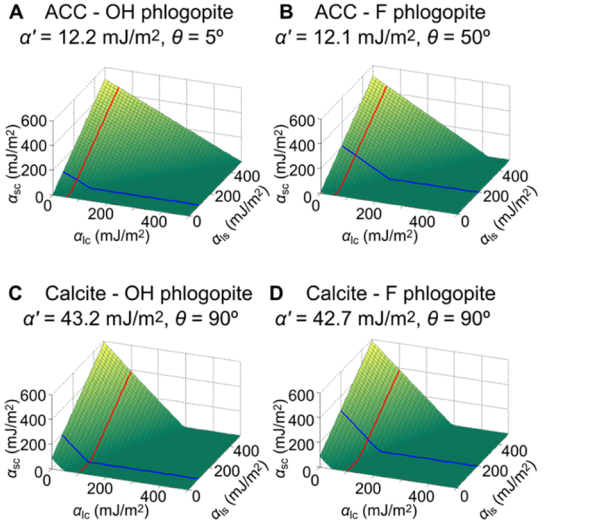

Figure 7. Interfacial free-energy surfaces for (A) ACC−OH phlogopite system, (B) ACC−F phlogopite system, (C) calcite−OH phlogopite system, and (D) calcite−F phlogopite system. The value of α_{sc} (substrate−crystal) is plotted as a function of different values for α_{lc} (liquid−crystal) and α_{ls} (liquid−substrate), using the value of the effective interfacial energy α' obtained from the GISAXS experiments. θ was set as 5° and 90° for ACC and calcite, respectively, for OH phlogopite and 50° and 90° for ACC and calcite, respectively, for F phlogopite. The red and the blue lines refer to representative values found in the literature.

plotted for each system using eq 4. These diagrams allow evaluating the interfacial free energy between the crystal and substrate (α_{sc}) as a function of the other two interfacial free-energy terms while making certain assumptions (see the Supporting Information).

The diagrams show that the observed stability of ACC on the hydrophilic substrate can indeed have a thermodynamic origin: the α_{sc} value (crossing point of the red and blue lines obtained based on the literature values; see the Supporting Information) for ACC on OH phlogopite (Figure 7A) is found to be lower than that on F phlogopite (Figure 7B). In addition, for F phlogopite, this α_{sc} value for ACC (Figure 7B) is indeed higher than that for calcite on the same substrate (Figure 7D). This implies that there is another thermodynamic driver for crystallization of ACC (on F phlogopite) via minimization of all of the interfacial free energies: ACC is the first formed precipitate, but it readily crystallizes to calcite so that the value of α_{sc} is minimized. For the OH system (Figure 7A,C), the α_{sc} value for calcite on the OH phlogopite is negative (negative values in Figure 7 have been set to zero), which indicates a nonphysical situation. In fact, as long as $\alpha_{lc\text{-}ACC} < \alpha_{lc\text{-}calcite}$ holds, which seems to be a reasonable assumption, α_{sc} is always found to be lower for calcite than for ACC when $\alpha_{ls} = 100$ mJ/m^2. This would also have occurred for F phlogopite if a higher value of α_{lc} was selected, although the energetic preference for calcite over ACC would not have changed. Given the absence of calcite on OH phlogopite according to FTIR observations

DOI: 10.1021/acs.chemmater.9b00417
Chem. Mater. 2019, 31, 3340−3348

(Figure 5B), this nonphysical situation (Figure 7C) may infer that (i) calcite cannot nucleate directly on OH phlogopite and its formation always proceeds via an amorphous intermediate (ACC) or that (ii) wrong estimations for α_{ls} and α_{lc} are being used. The uncertainties in the values of all of the interfacial free energies selected from the literature prevent us from giving more weight to one of these two possibilities, and thus both remain equally plausible. Nevertheless, nucleation of ACC should be more prone on OH phlogopite than on F phlogopite (Figure 7A,B) and the ACC formed on F phlogopite should crystallize readily (Figure 7B,D), which is observed in our experiments. Yet, sensitivity tests (data not shown) showed that the resulting interfacial energy values are more sensitive to the θ values than to the α' values. Increasing α' is followed by an incremental increase in the slope of the 3D surface, whereas increasing θ is followed by a more abrupt change in the tilt of the surface, which limits or extends the range of nonphysical values of α_{sc}.

The simplistic interfacial free-energy surfaces proposed here may not capture the whole complexity of the $CaCO_3$ system. The distinctive crystallization kinetics and the identical values for the effective interfacial free energies manifest the high "structural flexibility" of the $CaCO_3$ system, allowing it to nucleate on substrates with contrasting wetting properties. This ability to adapt to the substrate properties may indeed be part of the structural flexibility manifested as in different binding conformations, thus different energetic minima, occurring in the $CaCO_3$ crystals themselves. For instance, Ca^{2+} and CO_3^{2-} can bind through either monodentate (one oxygen atom shared) or bidentate (two oxygen atoms shared) ligands and each polymorph is known to have different proportions of such ligands (100% monodentate in calcite and ~50% in ACC and aragonite). The binding structure of $CaCO_3$ units is also different for hydrous polymorphs. Isolated hydrated ion pairs are present in the ikaite structure, whereas one H_2O molecule is hosted by each $CaCO_3$ unit in monohydrocalcite. In addition to this, the inherent structural disorder of ACC can increase its stereochemical adaptability to different substrate environments. Such a structural flexibility should therefore lead to a complex potential energy surface with certainly more than one local minimum in the configurational space, supporting in turn the observed adaptability to remarkably different environments such as those provided by OH and F phlogopite substrates, as shown in the present study. Perhaps, a system bearing no poly(a)-morphs such as NaCl can be a good candidate to discern this hypothesized "structural flexibility" as one of the major parameters governing the pathways and ability to nucleate heterogeneously.

CONCLUSIONS

Surface-mediated nucleation is a ubiquitous process for a number of natural and industrial processes such as biomineralization, subsurface reactive transport, and scale formation. It has generally been accepted that the hydrophobicity of the substrate controls the heterogeneous nucleation behavior by modulating the height of the nucleation barrier. However, and contrary to this hypothesis, we show that the effective interfacial energies, and therefore the energetic barriers, are similar for both the OH and F phlogopite. Irrespective of the substrate wetting properties, ACC is the first observed phase formed on both systems. Interestingly, however, it is the surface wetting properties that control crystallization kinetics. The hydrophilic substrate enhanced the kinetic persistence of ACC as compared to the less hydrophilic substrate, presumably by interactions between the water molecules of ACC and the hydrophilic substrate. In addition, ACC is also thermodynamically stabilized by the reduction of the interfacial penalty between the nuclei and substrate (α_{sc}).

Overall, this study successfully demonstrates the effect of surface wetting alone, excluding the ambiguity arising from stereochemical effects or lattice match, on the heterogeneous nucleation processes of $CaCO_3$. Even though the system proposed, that is, phlogopite, is purely abiotic, our results clearly show how materials wetting properties can have a striking control of the crystallization kinetics. This finding may be relevant to the nucleation processes of other systems and shed light on the further understanding of biomineralization mechanisms as well as on the design of biomimetic materials.

ASSOCIATED CONTENT

Supporting Information

The Supporting Information is available free of charge on the ACS Publications website at DOI: 10.1021/acs.chemmater.9b00417.

Additional data for GISAXS scattered intensity and AFM measurements, supplementary FTIR spectra obtained under various conditions as well as explanations on GISAXS setup, and assumptions used for Figure 7 (PDF)

AUTHOR INFORMATION

Corresponding Author

*E-mail: Alex.Fernandez-Martinez@univ-grenoble-alpes.fr.

ORCID

Alejandro Fernandez-Martinez: 0000-0001-5073-9629
Alexander E. S. Van Driessche: 0000-0003-2528-3425
Carlos M. Pina: 0000-0002-7748-5240
Byeongdu Lee: 0000-0003-2514-8805

Present Address

#Department of Civil and Environmental Engineering, Princeton University, Princeton, New Jersey 08544, United States.

Notes

The authors declare no competing financial interest.

ACKNOWLEDGMENTS

The authors thank Jussieu Collection, National Museum of Natural History (Paris, France) and H. C. Materials Corporation (IL, USA) for kindly providing the mineral samples as well as IRSTEA (Grenoble, France) for the use of FTIR spectroscopy. 12-ID-B at Advanced Photon Sources is acknowledged for the allocation of beamtime. This research was supported by French ministerial PhD scholarship, EC2CO (CNRS-INSU) NUCLEATION program, as well as Labex OSUG@2020 (Investissements d'avenir—ANR10 LABX56).

REFERENCES

(1) Sigg, L.; Stumm, W.; Behra, P. *CHIMIE DES MILIEUX AQUATIQUES: Chimie Des Eaux Naturelles et Des Interfaces Dans l'Environnement*; Masson: Paris, 1992.

(2) McCarthy, J. F.; Zachara, J. M. Subsurface transport of contaminants. *Environ. Sci. Technol.* **1989**, *23*, 496—502.

DOI: 10.1021/acs.chemmater.9b00417
Chem. Mater. 2019, 31, 3340—3348

(3) Fujita, Y.; Ferris, F. G.; Lawson, R. D.; Colwell, F. S.; Smith, R. W. Subscribed Content Calcium Carbonate Precipitation by Ureolytic Subsurface Bacteria. *Geomicrobiol. J.* **2000**, *17*, 305−318.
(4) Warren, L. A.; Maurice, P. A.; Parmar, N.; Ferris, F. G. Microbially Mediated Calcium Carbonate Precipitation: Implications for Interpreting Calcite Precipitation and for Solid-Phase Capture of Inorganic Contaminants. *Geomicrobiol. J.* **2001**, *18*, 93−115.
(5) Dong, W.; Ball, W. P.; Liu, C.; Wang, Z.; Stone, A. T.; Bai, J.; Zachara, J. M. Influence of Calcite and Dissolved Calcium on Uranium(VI) Sorption to a Hanford Subsurface Sediment. *Environ. Sci. Technol.* **2005**, *39*, 7949−7955.
(6) Lowenstam, H. A.; Weiner, S. *On Biomineralization*; Oxford University Press: New York, 1989.
(7) Sanders, R.; Henson, S. Ecological Carbon Sequestration in the Oceans and Climate Change. In *Global Environmental Change*; Freedman, B., Ed.; Springer: Dordrecht, 2014; pp 125−131.
(8) Morse, J. W.; Arvidson, R. S.; Lüttge, A. Calcium Carbonate Formation and Dissolution. *Chem. Rev.* **2007**, *107*, 342−381.
(9) Kashchiev, D. *Nucleation: Basic Theory with Applications*; Butterworth-Heinemann: Oxford, 2000.
(10) Debenedetti, P. G. *Metastable Liquids: Concepts and Principles*; Princeton University Press: Princeton, 1996.
(11) *New Perspectives on Mineral Nucleation and Growth: From Solution Precursors to Solid Materials*; Van Driessche, A. E. S., Kellermeier, M., Benning, L. G., Gebauer, D., Eds.; Springer International Publishing, 2017.
(12) Gebauer, D.; Völkel, A.; Cölfen, H.; Volkel, A.; Colfen, H. Stable Prenucleation Calcium Carbonate Clusters. *Science* **2008**, *322*, 1819−1822.
(13) De Yoreo, J. J.; Gilbert, P. U. P. A.; Sommerdijk, N. A. J. M.; Penn, R. L.; Whitelam, S.; Joester, D.; Zhang, H.; Rimer, J. D.; Navrotsky, A.; Banfield, J. F.; et al. Crystallization by Particle Attachment in Synthetic, Biogenic, and Geologic Environments. *Science* **2015**, *349*, aaa6760.
(14) Mass, T.; Giuffre, A. J.; Sun, C.-Y.; Stifler, C. A.; Frazier, M. J.; Neder, M.; Tamura, N.; Stan, C. V.; Marcus, M. A.; Gilbert, P. U. P. A. Amorphous Calcium Carbonate Particles Form Coral Skeletons. *Proc. Natl. Acad. Sci. U.S.A.* **2017**, *114*, E7670−E7678.
(15) Beniash, E.; Aizenberg, J.; Addadi, L.; Weiner, S. Amorphous Calcium Carbonate Transforms into Calcite during Sea Urchin Larval Spicule Growth. *Proc. R. Soc. London, Ser. B* **1997**, *264*, 461−465.
(16) Politi, Y.; Arad, T.; Klein, E.; Weiner, S.; Addadi, L. Sea Urchin Spine Calcite Forms via a Transient Amorphous Calcium Carbonate Phase. *Science* **2004**, *306*, 1161−1164.
(17) Weiss, I. M.; Tuross, N.; Addadi, L.; Weiner, S. Mollusc Larval Shell Formation: Amorphous Calcium Carbonate Is a Precursor Phase for Aragonite. *J. Exp. Zool.* **2002**, *293*, 478−491.
(18) Weiner, S.; Levi-Kalisman, Y.; Raz, S.; Addadi, L. Biologically Formed Amorphous Calcium Carbonate. *Connect. Tissue Res.* **2003**, *44*, 214−218.
(19) Addadi, L.; Raz, S.; Weiner, S. Taking Advantage of Disorder: Amorphous Calcium Carbonate and Its Roles in Biomineralization. *Adv. Mater.* **2003**, *15*, 959−970.
(20) Marsh, M. E. Regulation of CaCO3formation in Coccolithophores. *Comp. Biochem. Physiol., Part B: Biochem. Mol. Biol.* **2003**, *136*, 743−754.
(21) Gong, Y. U. T.; Killian, C. E.; Olson, I. C.; Appathurai, N. P.; Amasino, A. L.; Martin, M. C.; Holt, L. J.; Wilt, F. H.; Gilbert, P. U. P. A. Phase Transitions in Biogenic Amorphous Calcium Carbonate. *Proc. Natl. Acad. Sci. U.S.A.* **2012**, *109*, 6088−6093.
(22) Shechter, A.; Glazer, L.; Cheled, S.; Mor, E.; Weil, S.; Berman, A.; Bentov, S.; Aflalo, E. D.; Khalaila, I.; Sagi, A. A Gastrolith Protein Serving a Dual Role in the Formation of an Amorphous Mineral Containing Extracellular Matrix. *Proc. Natl. Acad. Sci. U.S.A.* **2008**, *105*, 7129−7134.
(23) Bentov, S.; Weil, S.; Glazer, L.; Sagi, A.; Berman, A. Stabilization of Amorphous Calcium Carbonate by Phosphate Rich Organic Matrix Proteins and by Single Phosphoamino Acids. *J. Struct. Biol.* **2010**, *171*, 207−215.
(24) Whittaker, M. L.; Dove, P. M.; Joester, D. Nucleation on Surfaces and in Confinement. *MRS Bull.* **2016**, *41*, 388−392.
(25) Tester, C. C.; Whittaker, M. L.; Joester, D. Controlling Nucleation in Giant Liposomes. *Chem. Commun.* **2014**, *50*, 5619−5622.
(26) Pouget, E. M.; Bomans, P. H. H.; Goos, J. A. C. M.; Frederik, P. M.; de With, G. The Initial Stages of Template-Controlled CaCO3 Formation Revealed by Cryo-TEM. *Science* **2009**, *323*, 1455−1458.
(27) Sommerdijk, S. L.; Rosso, K. M.; Kerisit, S. N. Nucleation and Epitaxy-Mediated Phase Transformation of a Precursor Cadmium Carbonate Phase at the Calcite/Water Interface. *J. Phys. Chem. C* **2017**, *121*, 5012−5019.
(28) Chiquet, P.; Broseta, D.; Thibeau, S. Wettability Alteration of Caprock Minerals by Carbon Dioxide. *Geofluids* **2007**, *7*, 112−122.
(29) Espinoza, D. N.; Santamarina, J. C. Water-CO2-Mineral Systems: Interfacial Tension, Contact Angle, and DiffusionImplications to CO2 Geological Storage. *Water Resour. Res.* **2010**, *46*, W07537.
(30) Chen, T.; Neville, A.; Yuan, M. Calcium Carbonate Scale Formation - Assessing the Initial Stages of Precipitation and Deposition. *J. Pet. Sci. Eng.* **2005**, *46*, 185−194.
(31) Yang, Q.; Liu, Y.; Gu, A.; Ding, J.; Shen, Z. Investigation of Calcium Carbonate Scaling Inhibition and Scale Morphology by AFM. *J. Colloid Interface Sci.* **2001**, *240*, 608−621.
(32) Söhnel, O.; Garside, J. *Precipitation—Basic Principles and Industrial Applications*; Butterworth-Heinemann: Oxford, 1992.
(33) Sommerdijk, N. A. J. M.; With, G. d. Biomimetic CaCO3 Mineralization Using Designer Molecules and Interfaces. *Chem. Rev.* **2008**, *108*, 4499−4550.
(34) Aizenberg, J. New Nanofabrication Strategies: Inspired by Biomineralization. *MRS Bull.* **2010**, *35*, 323−330.
(35) Meyers, M. A.; McKittrick, J.; Chen, P.-Y. Structural Biological Materials: Critical Mechanics-Materials Connections. *Science* **2013**, *339*, 773−779.
(36) Turnbull, D.; Vonnegut, B. Nucleation Catalysis. *Ind. Eng. Chem.* **1952**, *44*, 1292−1298.
(37) Dai, C.; Stack, A. G.; Koishi, A.; Fernandez-Martinez, A.; Lee, S. S.; Hu, Y. Heterogeneous Nucleation and Growth of Barium Sulfate at Organic−Water Interfaces: Interplay between Surface Hydrophobicity and Ba 2+ Adsorption. *Langmuir* **2016**, *32*, 5277−5284.
(38) Giuffre, A. J.; Hamm, L. M.; Han, N.; De Yoreo, J. J.; Dove, P. M. Polysaccharide Chemistry Regulates Kinetics of Calcite Nucleation through Competition of Interfacial Energies. *Proc. Natl. Acad. Sci. U.S.A.* **2013**, *110*, 9261−9266.
(39) Smeets, P. J. M.; Cho, K. R.; Kempen, R. G. E.; Sommerdijk, N. a. J. M.; De Yoreo, J. J. Calcium Carbonate Nucleation Driven by Ion Binding in a Biomimetic Matrix Revealed by in Situ Electron Microscopy. *Nat. Mater.* **2015**, *14*, 394−399.
(40) Hamm, L. M.; Giuffre, A. J.; Han, N.; Tao, J.; Wang, D.; De Yoreo, J. J.; Dove, P. M. Reconciling Disparate Views of Template-Directed Nucleation through Measurement of Calcite Nucleation Kinetics and Binding Energies. *Proc. Natl. Acad. Sci. U.S.A.* **2014**, *111*, 1304−1309.
(41) Li, Q.; Fernandez-Martinez, A.; Lee, B.; Waychunas, G. A.; Jun, Y.-S. Interfacial Energies for Heterogeneous Nucleation of Calcium Carbonate on Mica and Quartz. *Environ. Sci. Technol.* **2014**, *48*, 5745−5753.
(42) Fernandez-Martinez, A.; Hu, Y.; Lee, B.; Jun, Y.-S.; Waychunas, G. A. In Situ Determination of Interfacial Energies between Heterogeneously Nucleated CaCO3 and Quartz Substrates: Thermodynamics of CO2 Mineral Trapping. *Environ. Sci. Technol.* **2013**, *47*, 102−109.
(43) Parkhurst, B. D. L.; Appelo, C. A. J. User's Guide To PHREEQC (Version 2) — a Computer Program for Speciation, and Inverse Geochemical Calculations. *Water-Resources Investigations Report 99-4259*; U.S. Geological Survey, 1999.
(44) Plummer, L. N.; Busenberg, E. The Solubilities of Calcite, Aragonite and Vaterite in CO2-H2O Solutions between 0 and 90°C,

DOI: 10.1021/acs.chemmater.9b00417
Chem. Mater. 2019, 31, 3340−3348

and an Evaluation of the Aqueous Model for the System CaCO3-CO2-H2O. *Geochim. Cosmochim. Acta* **1982**, *46*, 1011−1040.
(45) Kellermeier, M.; Picker, A.; Kempter, A.; Cölfen, H.; Gebauer, D. A Straightforward Treatment of Activity in Aqueous CaCo3 Solutions and the Consequences for Nucleation Theory. *Adv. Mater.* **2014**, *26*, 752−757.
(46) Renaud, G.; Lazzari, R.; Leroy, F. Probing Surface and Interface Morphology with Grazing Incidence Small Angle X-Ray Scattering. *Surf. Sci. Rep.* **2009**, *64*, 255−380.
(47) Beaucage, G.; Kammler, H. K.; Pratsinis, S. E. Particle Size Distributions from Small-Angle Scattering Using Global Scattering Functions. *J. Appl. Crystallogr.* **2004**, *37*, 523−535.
(48) Beaucage, G. Small-Angle Scattering from Polymeric Mass Fractals of Arbitrary Mass-Fractal Dimension. *J. Appl. Crystallogr.* **1996**, *29*, 134−146.
(49) Markgraf, S. A.; Reeder, R. J. High-Temperature Structure Refinements of Calcite and Magnesite. *Am. Mineral.* **1985**, *70*, 590−600.
(50) Fernandez-Martinez, A.; Kalkan, B.; Clark, S. M.; Waychunas, G. a. Pressure-Induced Polyamorphism and Formation of "aragonitic" Amorphous Calcium Carbonate. *Angew. Chem., Int. Ed.* **2013**, *52*, 8354−8357.
(51) Horcas, I.; Fernández, R.; Gomez-Rodriguez, J. M.; Colchero, J.; Gomez-Herrero, J.; Baro, A. M. WSXM: A Software for Scanning Probe Microscopy and a Tool for Nanotechnology. *Rev. Sci. Instrum.* **2007**, *78*, 013705.
(52) *Springer Handbook of Nanotechnology*, 2nd ed.; Bhushan, B., Ed.; Springer: Berlin, 2007.
(53) Kuwahara, Y. Comparison of the Surface Structure of the Tetrahedral Sheets of Muscovite and Phlogopite by AFM. *Phys. Chem. Miner.* **2001**, *28*, 1−8.
(54) Sijakova-Ivanova, T.; Cukovska, L. R. Mineralogical Characteristics of Phlogopite from Dupen Kamen, Republic of Macedonia. *IOSR J. Appl. Geol. Geophys.* **2016**, *04*, 72−76.
(55) Šontevska, V.; Jovanovski, G.; Makreski, P.; Raškovska, A.; Šoptrajanov, B. Minerals from Macedonia. XXI. Vibrational Spectroscopy as Identificational Tool for Some Phyllosilicate Minerals. *Acta Chim. Slov.* **2008**, *55*, 757−766.
(56) Gianfagna, A.; Scordari, F.; Mazziotti-Tagliani, S.; Ventruti, G.; Ottolini, L. Fluorophlogopite from Biancavilla (Mt. Etna, Sicily, Italy): Crystal Structure and Crystal Chemistry of a New F-Dominant Analog of Phlogopite. *Am. Mineral.* **2007**, *92*, 1601−1609.
(57) Scordari, F.; Schingaro, E.; Ventruti, G.; Nicotra, E.; Viccaro, M.; Tagliani, S. M. Fluorophlogopite from Piano Delle Concazze (Mt. Etna, Italy): Crystal Chemistry and Implications for the Crystallization Conditions. *Am. Mineral.* **2013**, *98*, 1017−1025.
(58) Hodson, M. E.; Benning, L. G.; Demarchi, B.; Penkman, K. E. H.; Rodriguez-Blanco, J. D.; Schofield, P. F.; Versteegh, E. A. A. Biomineralisation by Earthworms - an Investigation into the Stability and Distribution of Amorphous Calcium Carbonate. *Geochem. Trans.* **2015**, *16*, 4.
(59) Demény, A.; Németh, P.; Czuppon, G.; Leél-Őssy, S.; Szabó, M.; Judik, K.; Németh, T.; Stieber, J. Formation of Amorphous Calcium Carbonate in Caves and Its Implications for Speleothem Research. *Sci. Rep.* **2016**, *6*, 39602.
(60) Loste, E.; Wilson, R. M.; Seshadri, R.; Meldrum, F. C. The Role of Magnesium in Stabilising Amorphous Calcium Carbonate and Controlling Calcite Morphologies. *J. Cryst. Growth* **2003**, *254*, 206−218.
(61) Rodriguez-Blanco, J. D.; Shaw, S.; Benning, L. G. The Kinetics and Mechanisms of Amorphous Calcium Carbonate (ACC) Crystallization to Calcite, Viavaterite. *Nanoscale* **2011**, *3*, 265−271.
(62) Fleet, M. E.; Liu, X.; King, P. L. Accommodation of the Carbonate Ion in Apatite: An FTIR and X-Ray Structure Study of Crystals Synthesized at 2-4 GPa. *Am. Mineral.* **2004**, *89*, 1422−1432.
(63) Sato, M.; Matsuda, S. Structure of Vaterite and Infrared Spectra. *Z. Kristallogr.* **1969**, *129*, 405−410.
(64) Noel, E. H.; Kim, Y.-Y.; Charnock, J. M.; Meldrum, F. C. Solid State Crystallization of Amorphous Calcium Carbonate Nanoparticles Leads to Polymorph Selectivity. *CrystEngComm* **2013**, *15*, 697−705.
(65) Schaefer, D. W. Polymers, Fractals, and Ceramic Materials. *Science* **1989**, *243*, 1023−1027.
(66) Pouget, E. M.; Bomans, P. H. H.; Dey, A.; Frederik, P. M.; de With, G.; Sommerdijk, N. A. J. M. The Development of Morphology and Structure in Hexagonal Vaterite. *J. Am. Chem. Soc.* **2010**, *132*, 11560−11565.
(67) Radha, A. V.; Forbes, T. Z.; Killian, C. E.; Gilbert, P. U. P. A.; Navrotsky, A. Transformation and Crystallization Energetics of Synthetic and Biogenic Amorphous Calcium Carbonate. *Proc. Natl. Acad. Sci. U.S.A.* **2010**, *107*, 16438−16443.
(68) Xiao, J.; Wang, Z.; Tang, Y.; Yang, S. Biomimetic Mineralization of CaCO3 on a Phospholipid Monolayer: From an Amorphous Calcium Carbonate Precursor to Calcite via Vaterite. *Langmuir* **2010**, *26*, 4977−4983.

DOI: 10.1021/acs.chemmater.9b00417
Chem. Mater. 2019, 31, 3340−3348